Electronic Supplementary Information

Crystal Phase-Tailored Metal Heterojunction for Dual-Site Acceleration of Alkaline Hydrogen Evolution

Leyang Song,‡ Yushuang Gong,‡ Xiang Liu, Shiling Yuan and An-Liang Wang*

Key Laboratory for Colloid and Interface Chemistry, Ministry of Education, School of Chemistry and Chemical Engineering, Shandong University, Jinan 250100, Shandong, China.

‡These authors contributed equally to this work.

*Corresponding author.

Email: alwang@sdu.edu.cn.

Experimental Section

Text S1. Chemicals

Nickel (II) acetylacetonate ($Ni(acac)_2$, 95 wt%), polyethyleneimine (PEI, M.W. 18000, 99 wt%), and potassium hydroxide (KOH, 90 wt%), tert-butyl alcohol (TBA, ≥99.0 wt%) were purchased from Shanghai Macklin Biochemical Co., Ltd. N, N-dimethylformamide (DMF, C_3H_7NO, ≥99.5 wt%) was purchased from Shanghai Aladdin Biochemical Technology Co., Ltd. Ethanol (C_2H_5OH, ≥99.7 wt%) was bought from Tianjin Fuyu Fine Chemical Co., Ltd. Chloroform ($CHCl_3$, ≥99.0 wt%) and hydrochloric acid (HCl, 36.0-38.0 wt%) was bought from Yantai Yuandong Fine Chemical Co., Ltd. Rhodium (III) chloride hydrate ($RhCl_3 \cdot xH_2O$, 99 wt%) was obtained from Shanghai Bide Pharmatech Co., Ltd. Nafion solution (5 wt%) was obtained from Dupont. Pt/C (20 wt%, HISPEC3000, Johnson Matthey) was purchased from Suzhou Yilongsheng Energy Technology Co., Ltd. Potassium deuteroxide (KOD, 30 wt% in D_2O) was purchased from Anhui Senrise Technology Co., Ltd. Deuterium oxide (D_2O, 99.9 at% D) was purchased from Wuhan Isotope Technology Co., Ltd. Carbon paper (CP) was bought from Suzhou Sinero Technology Co., Ltd. All chemicals were used without further purification.

Text S2. Materials synthesis

Synthesis of hexagonal close-packed (hcp) Ni

A mixture containing 150 mg of $Ni(acac)_2$ and 0.6 g of PEI was dissolved in 11 mL of DMF to form a solution by stirring. Subsequently, the solution was transferred into a polytetrafluoroethylene (PTFE)-lined stainless-steel autoclave. The autoclave was heated at 200 ℃ for 24 h. After cooling to room temperature, the resulting products were thoroughly washed with ethanol and chloroform.

Synthesis of hcp Ni/face-centered cubic (fcc) Rh

For the synthesis of hcp Ni/fcc Rh, 10 mg of hcp Ni and 15 mg of $RhCl_3 \cdot xH_2O$ were dissolved in 2 mL of deionized water. The resulting mixture was heated to 60 ℃ and reacted at this temperature for 1 h. The products were collected by centrifugation and washed with ethanol. Samples designated as hcp Ni/fcc Rh-3 h and hcp Ni/fcc Rh-5 h were prepared by extending the reaction time to 3 h and 5 h, respectively, while maintaining all other synthesis conditions.

Synthesis of fcc Ni/fcc Rh

Fcc Ni/fcc Rh was synthesized by annealing hcp Ni/fcc Rh at 400 ℃ for 1 h at Ar/H_2 atmosphere.

Synthesis of fcc Rh

The as-prepared hcp Ni/fcc Rh was immersed in 10 mL of concentrated hydrochloric acid within a glass bottle and kept at room temperature overnight. Subsequently, the fcc Rh sample was collected by centrifugation, washed sequentially with ethanol and deionized water.

Synthesis of NiFe layered double hydroxide (LDH)/NF

Ni foam (NF) was successively sonicated in 1.0 M HCl, ethanol, and deionized water. A solution was prepared by dissolving $Ni(NO_3)_2 \cdot 6H_2O$ (0.6979 g), $Fe(NO_3)_3 \cdot 9H_2O$ (0.3232 g), and urea (0.3003 g) in 35 mL of deionized water. This solution was then transferred to a 50 mL Teflon-lined stainless-steel autoclave. The pretreated NF (3×5 cm^2) was vertically immersed into the solution and the sealed autoclave was heated to 120 °C and maintained at this temperature for 12 h. After the reaction, the autoclave was allowed to cool naturally to room temperature. The resulting NiFe LDH on NF was washed alternately with deionized water and ethanol, and finally dried under vacuum at 60 °C overnight.

Text S3. Materials characterization

Crystal structures of all samples were characterized by using X-ray diffraction (XRD, SmartLab 9 kW) with Cu Kα radiation source (λ = 1.5418 Å). Morphological characterizations were conducted on a transmission electron microscope (TEM, HT-7700) and a high-resolution transmission electron microscope (HRTEM, JEOL 2100F). ESCALAB 250Xi instrument was used to record X-ray photoelectron spectroscopy (XPS) and C 1s peak at 284.8 eV was used as a standard to calibrate the data. The X-ray absorption near-edge structure (XANES) and extended X-ray absorption fine structure (EXAFS) spectra of Rh K-edge were performed at the BL14W1 station of Shanghai Synchrotron Radiation Facility, China. The inductively coupled plasma-optical emission spectroscopy (ICP-OES) was performed on an Agilent 5110 to determine the atomic ratio of Rh to Ni.

Text S4. Electrochemical measurements

All electrochemical measurements were conducted at room temperature using a standard three-electrode system on a CHI760E electrochemical workstation (Chenhua, Shanghai). Catalyst-loaded CP with electrocatalysts (Rh mass loading: 38 μg cm^{-2}) was used as the working electrode, a Hg/HgO electrode and a graphite rod served as the reference and counter electrodes, respectively. To prepare the catalyst ink, 4 mg of catalyst were homogeneously dispersed in a mixture containing 720 μL of ethanol, 240 μL of deionized water, and 40 μL of Nafion solution (5 wt%). For comparison, the

loading amount of commercial Pt/C was 190 μg cm^{-2}. All potentials were calibrated by reversible hydrogen electrode (RHE) using the following equation: ERHE = EHg/HgO + 0.059 × pH + 0.098, and were iR-corrected. Cyclic voltammogram (CV) were conducted in the non-faradaic reaction region at different sweep rates (20, 40, 60, 80, 100, 120 mV s^{-1}) to determine the double-layer capacitances (C_{dl}). The electrochemically active surface area (ECSA) was calculated from C_{dl} using the following equation:

$$ECSA = \frac{C_{dl}}{C_s} \#(1)$$

where C_s is the specific capacitance (0.040 mF cm^{-2}) of a smooth planar surface with 1.0 cm^2 surface area.[1]

Electrochemical impedance spectroscopy (EIS) was measured in a frequency range of 0.1-100000 Hz. The stability was assessed via chronopotentiometry at 100 mA cm^{-2}.

Text S5. Turnover frequency (TOF) value calculations

The TOF was calculated using the following equation:[2]

$$TOF = \frac{I}{2 n F} \#(2)$$

where I represents the current (A) obtained from the LSV curve, 2 stands for the number of electrons transferred to produce one H_2 molecular, n is the number of active sites, F is the Faraday constant (96485 C mol^{-1}).

Text S6. Faradaic efficiency (FE) of H_2 calculations

The FE was determined by comparing the experimentally collected amount of H_2 with the theoretical amount calculated from the passed charge (Q). The produced H_2 was quantitatively collected using a water drainage method in an H-type cell at a current density of 0.1 A cm^{-2}, and the gas volume was recorded every 10 min using an electrochemical workstation (Chenhua CHI760E). The FE was calculated using the following equations:

$$Q = I \times t \#(3)$$

$$FE\ (\%) = \frac{n \times F \times V}{Q \times V_m} \times 100\% \#(4)$$

where I is the applied current, t is the collection time, n is the number of electrons required to produce one H_2 molecule (n = 2), F is the Faraday constant, V is the experimentally measured volume of H_2, V_m is the molar volume of H_2, Q is the total charge passed.

Text S7. Kinetic isotope effect (KIE) calculations

The KIE was calculated using the following equation:[3]

$$KIE = \left|\frac{j_{H_2O}}{j_{D_2O}}\right|_{\eta} \#(5)$$

where j_{H_2O}, j_{D_2O} are the current densities measured in 1.0 M KOH/H_2O and 1.0 M KOD/D_2O, respectively, at the same overpotential (η).

Text S8. Activation energy calculations

The values of activation energy were calculated using the Arrhenius equation:[4]

$$j = A\, e^{-\frac{E_a}{RT}} \#(6)$$

The activation energy (E_a) was calculated using the following equation:

$$\left|\frac{\partial(\log_{10} j)}{\partial(1/T)}\right|_{\eta} = -\frac{E_a}{2.303\ R} \#(7)$$

where j is the current density at a constant potential, A is the apparent pre-exponential factor, R is the ideal gas constant (8.314 J K^{-1} mol^{-1}), T is the Kelvin temperature (K), E_a is the apparent activation energy.

Text S9. Anion exchange membrane water electrolyzer (AEMWE) tests

The AEMWE comprised an anode, a cathode, an anion exchange membrane (Fumasep FAA-3-PK), and bipolar plates. The cathode employed CP loaded with the hcp Ni/fcc Rh catalyst, NiFe LDH/NF served as the anode (hcp Ni/fcc Rh mass loading: 1 mg cm^{-2}; NiFe LDH mass loading: 1.6 mg cm^{-2}), while Ti fiber felt was used as the gas diffusion layer (GDL). The AEM was used to separate the anode and cathode compartments. The assembled device underwent electrochemical performance evaluation, including polarization curve and stability measurement in 1.0 M KOH at 50 ℃.

Text S10. Density functional theory (DFT) calculations

The DFT calculations were conducted on the Vienna ab-initio simulation package (VASP) software to obtain the interface models of the prepared materials.[5] The projector augmented wave (PAW) method with a cutoff energy of 400 eV accompanied by Perdew-Burke-Ernzerhof (PBE) functional was used in the DFT calculations.[6] The DFT-D3 method was incorporated into the calculations to correct for the van der Waals interactions.[7] According to the principle of the lowest surface energy facet and previous reports, the hcp Ni (001), fcc Ni (111), and fcc Rh (111) facets were chosen for the construction of structural model.[8-10] The energy convergence criterion was 10^{-5} eV and the force convergence criterion was 0.03 eV/Å. The Brillouin zone integration was performed with 3×3×1 Monkhorst-Pack k-point mesh in the structure optimization process. The Gibbs free energy (ΔG) of

each HER step can be obtained by the following equation:

$$\Delta G = \Delta E + \Delta ZPE - T\Delta S\# \quad (8)$$

where ΔE denotes the reaction energy difference, ΔZPE represents the zero-point energy, ΔS refers to the entropy (S) change between products and reactants, T is the reaction temperature (298.15 K).

Supplementary Figures

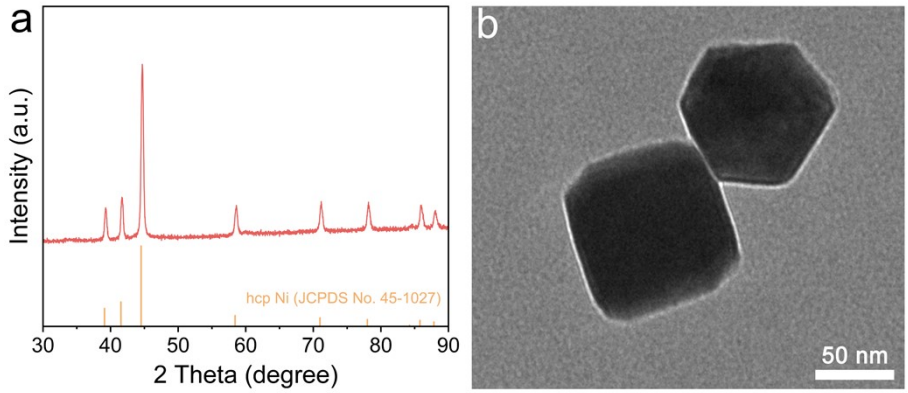

Fig. S1. (a) XRD pattern and (b) TEM image of hcp Ni.

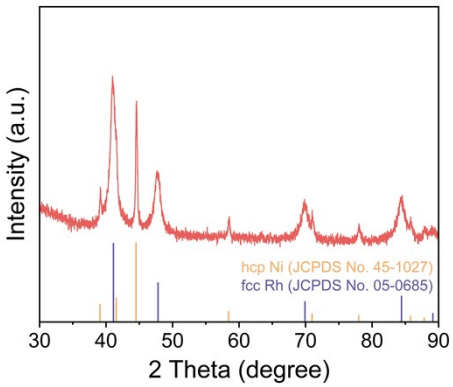

Fig. S2. XRD pattern of hcp Ni/fcc Rh.

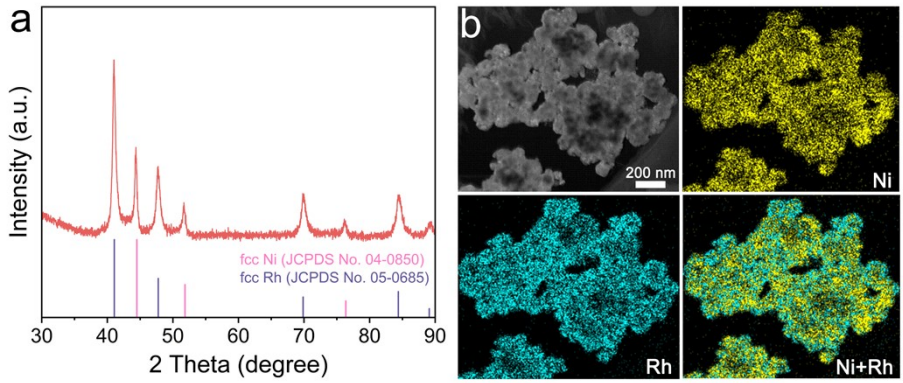

Fig. S3. (a) XRD pattern, (b) HAADF-STEM image and corresponding elemental mappings of fcc Ni/fcc Rh.

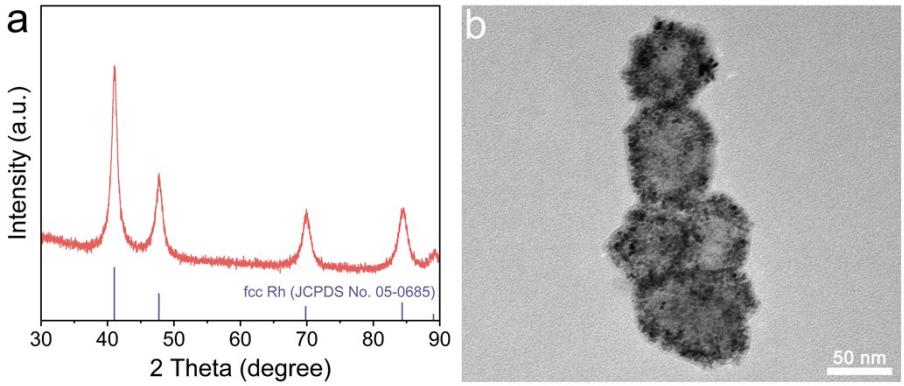

Fig. S4. (a) XRD pattern and (b) TEM image of fcc Rh.

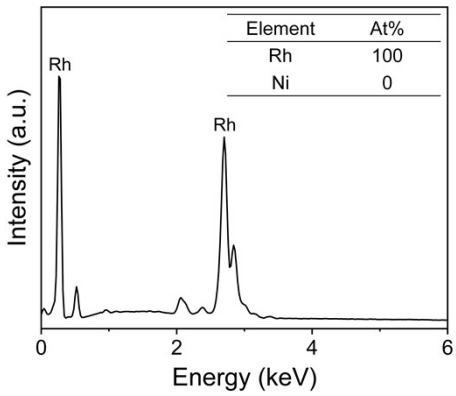

Fig. S5. EDS spectrum of fcc Rh.

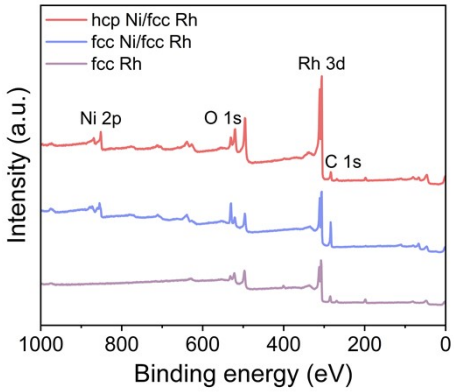

Fig. S6. XPS full survey spectra of hcp Ni/fcc Rh, fcc Ni/fcc Rh, and fcc Rh.

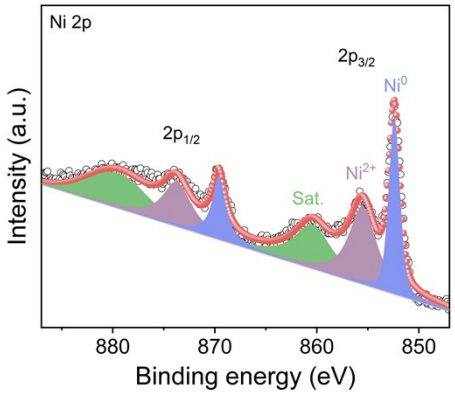

Fig. S7. High-resolution Ni 2p XPS spectrum of hcp Ni.

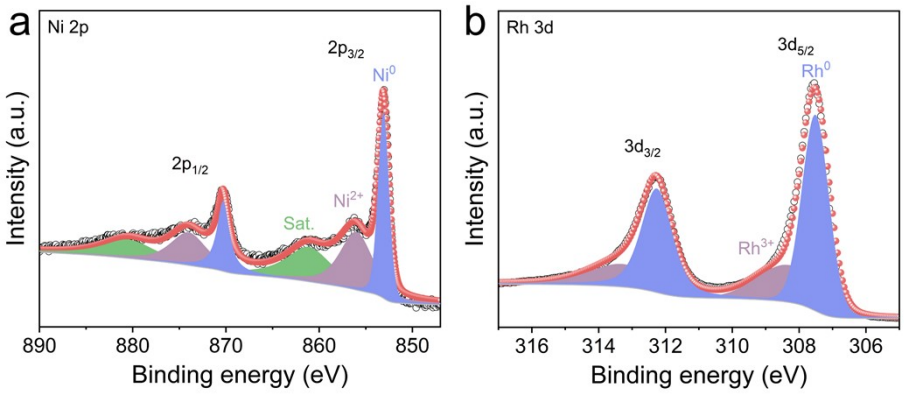

Fig. S8. High-resolution (a) Ni 2p and (b) Rh 3d XPS spectra of hcp Ni/fcc Rh.

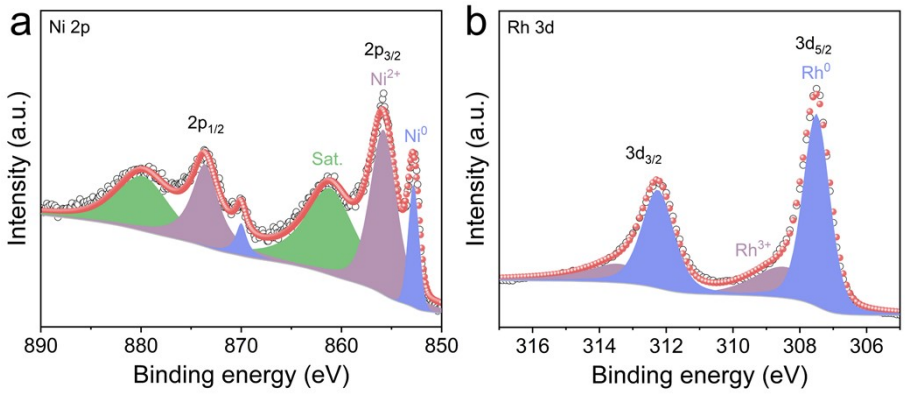

Fig. S9. High-resolution (a) Ni 2p and (b) Rh 3d XPS spectra of fcc Ni/fcc Rh.

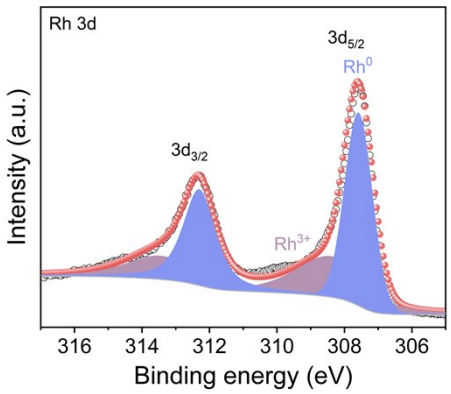

Fig. S10. High-resolution Rh 3d XPS spectrum of fcc Rh.

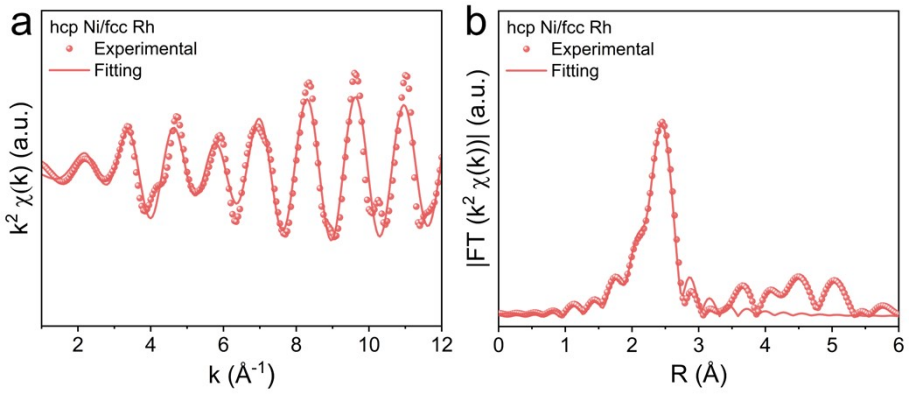

Fig. S11. Rh K-edge EXAFS fitting curves of hcp Ni/fcc Rh at (a) k space and (b) R space.

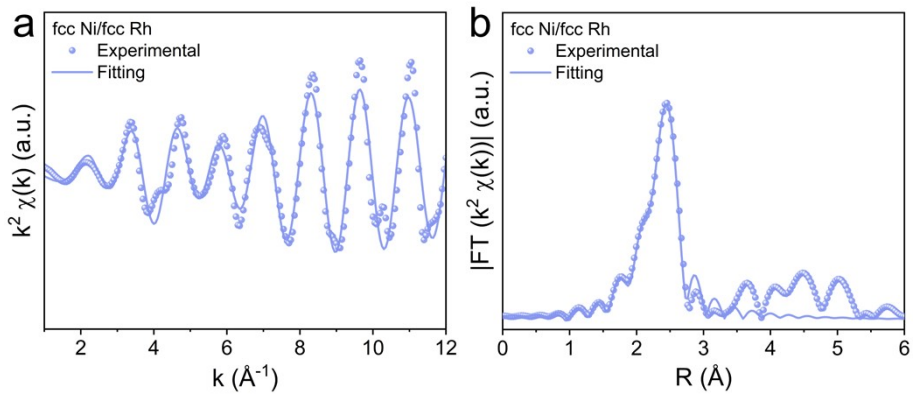

Fig. S12. Rh K-edge EXAFS fitting curves of fcc Ni/fcc Rh at (a) k space and (b) R space.

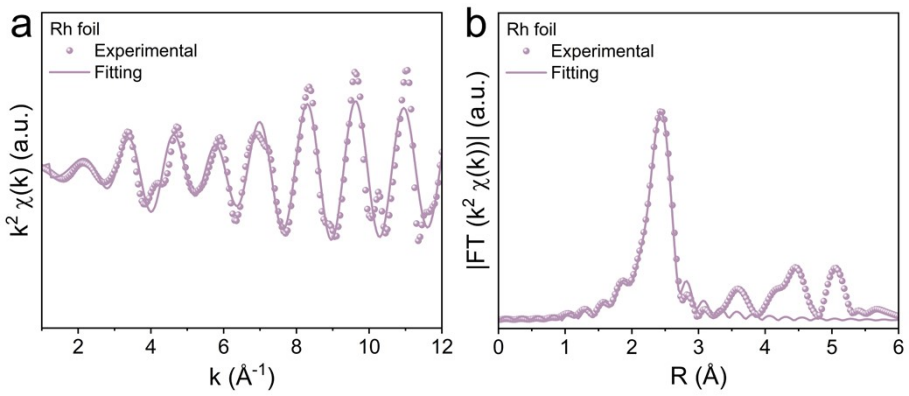

Fig. S13. Rh K-edge EXAFS fitting curves of Rh foil at (a) k space and (b) R space.

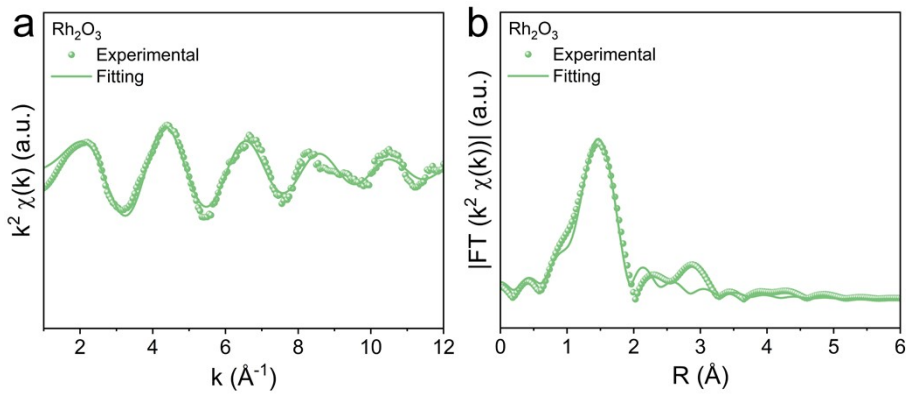

Fig. S14. Rh K-edge EXAFS fitting curves of Rh_2O_3 at (a) k space and (b) R space.

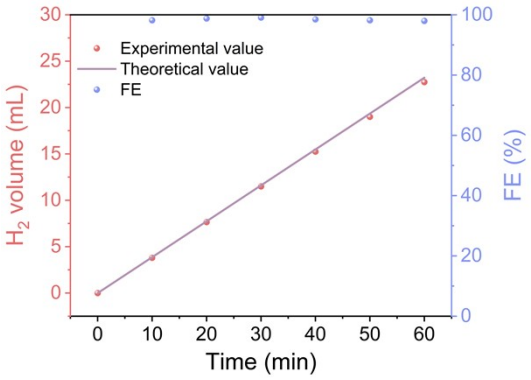

Fig. S15. The FE of hcp Ni/fcc Rh.

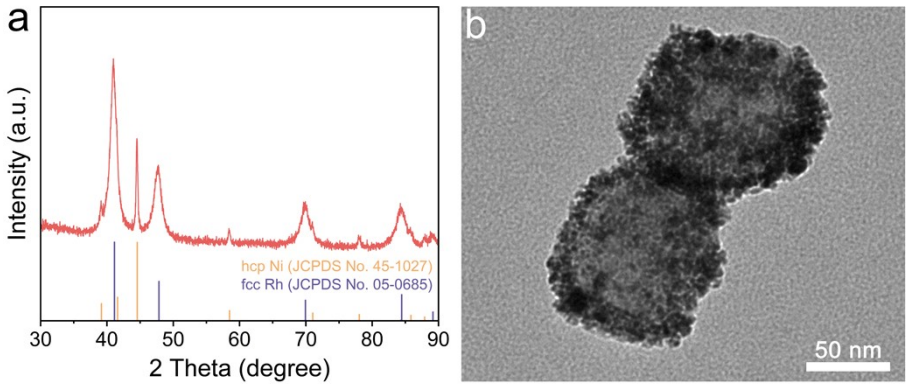

Fig. S16. (a) XRD pattern and (b) TEM image of hcp Ni/fcc Rh-3 h.

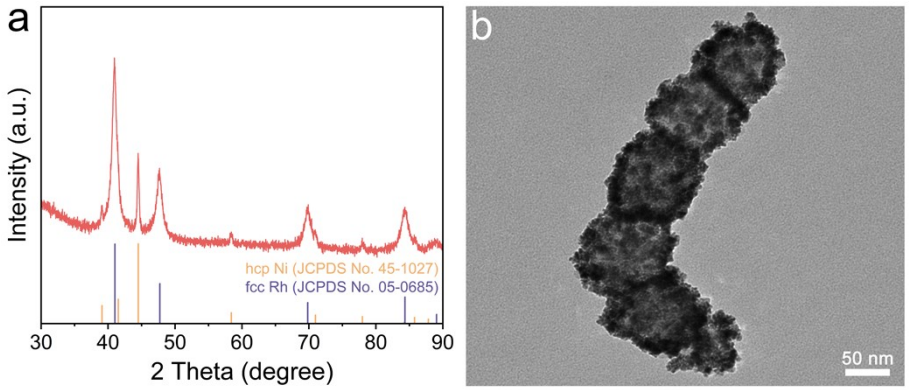

Fig. S17. (a) XRD pattern and (b) TEM image of hcp Ni/fcc Rh-5 h.

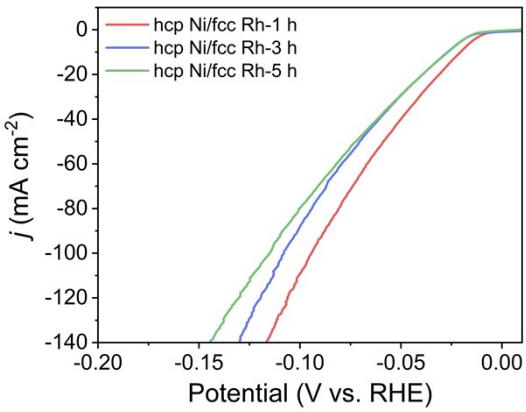

Fig. S18. Polarization curves of hcp Ni/fcc Rh-1 h, hcp Ni/fcc Rh-3 h, and hcp Ni/fcc Rh-5 h in 1.0 M KOH.

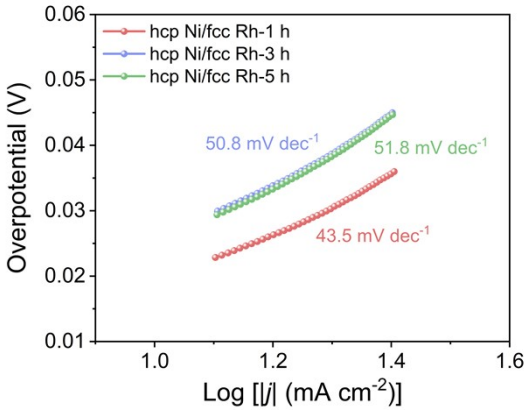

Fig. S19. Tafel slopes of hcp Ni/fcc Rh-1 h, hcp Ni/fcc Rh-3 h, and hcp Ni/fcc Rh-5 h.

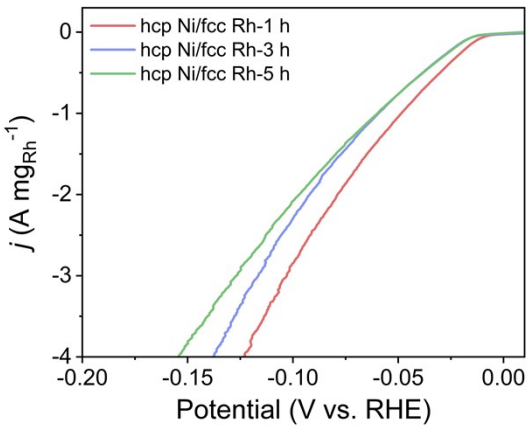

Fig. S20. Polarization curves (current density is normalized to Rh mass) of hcp Ni/fcc Rh-1 h, hcp Ni/fcc Rh-3 h, and hcp Ni/fcc Rh-5 h.

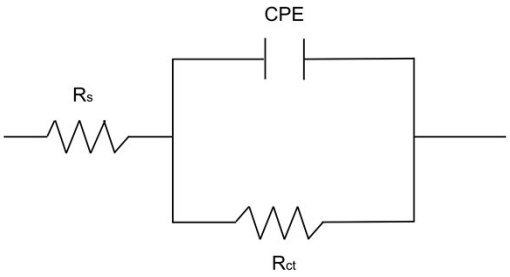

Fig. S21. The equivalent circuit model of EIS measurements for HER. R_s, R_{ct} and CPE represent solution resistance, charge transfer resistance and constant phase element, respectively.

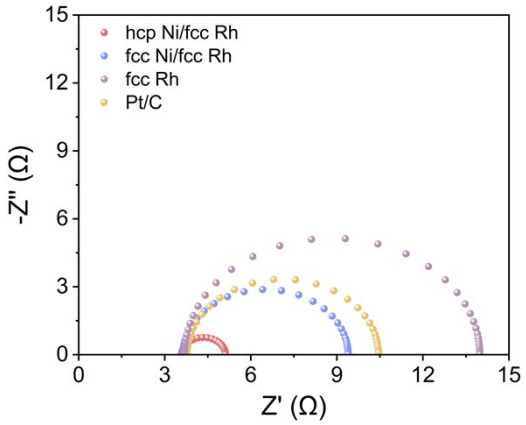

Fig. S22. EIS curves of hcp Ni/fcc Rh, fcc Ni/fcc Rh, fcc Rh, and Pt/C.

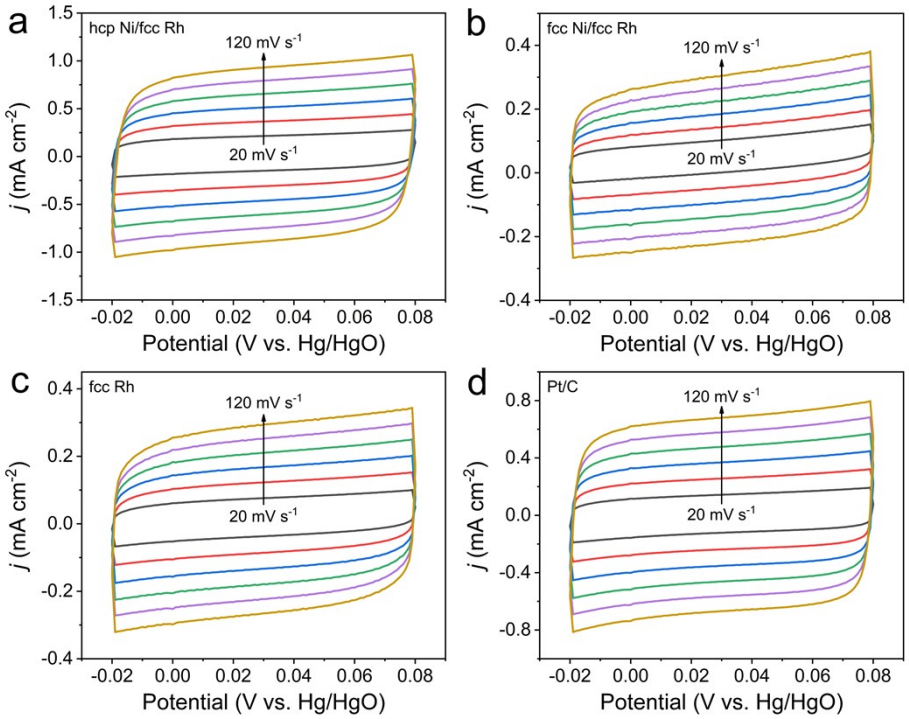

Fig. S23. CV curves of (a) hcp Ni/fcc Rh, (b) fcc Ni/fcc Rh, (c) fcc Rh, and (d) Pt/C at different scan rates from 20 mV s^{-1} to 120 mV s^{-1} in 1.0 M KOH.

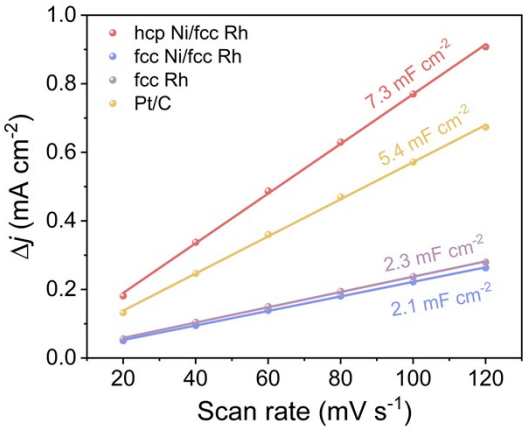

Fig. S24. Plots of the current density versus the scan rate for hcp Ni/fcc Rh, fcc Ni/fcc Rh, fcc Rh, and Pt/C.

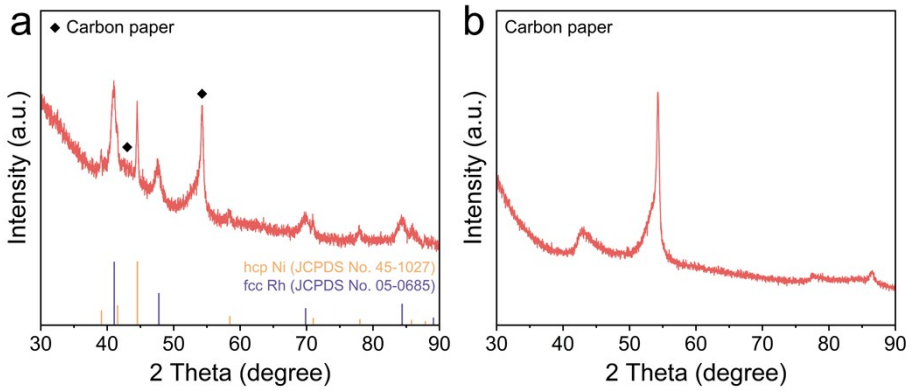

Fig. S25. XRD patterns of (a) hcp Ni/fcc Rh after stability test and (b) carbon paper.

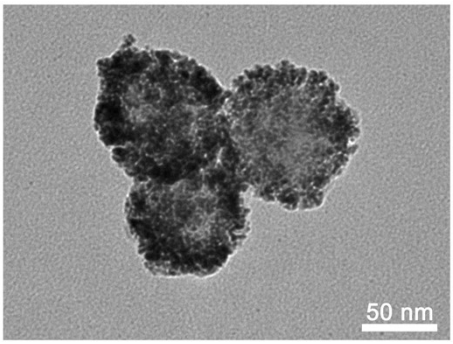

Fig. S26. TEM image of hcp Ni/fcc Rh after stability test.

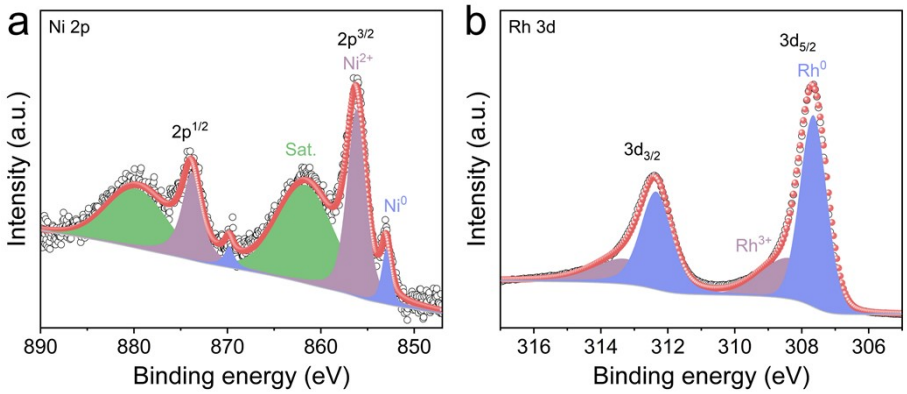

Fig. S27. High-resolution Ni 2p and Rh 3d XPS spectra of hcp Ni/fcc Rh after stability test.

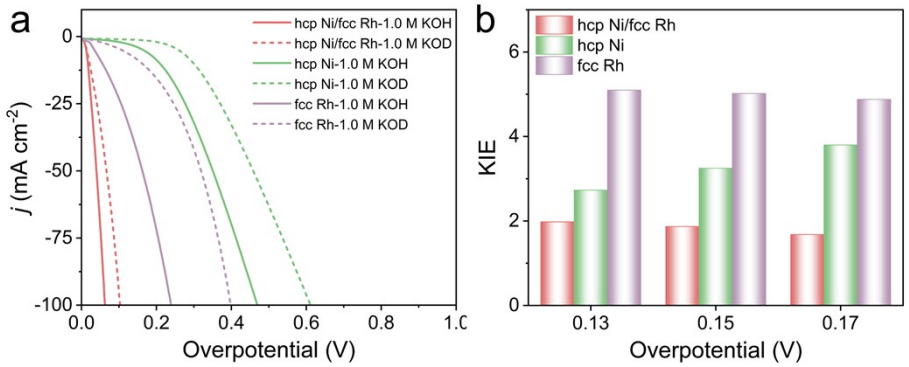

Fig. S28. (a) Polarization curves of hcp Ni/fcc Rh, hcp Ni, and fcc Rh in 1.0 M KOH/H_2O and KOD/D_2O. (b) KIE values of hcp Ni/fcc Rh, hcp Ni, and fcc Rh.

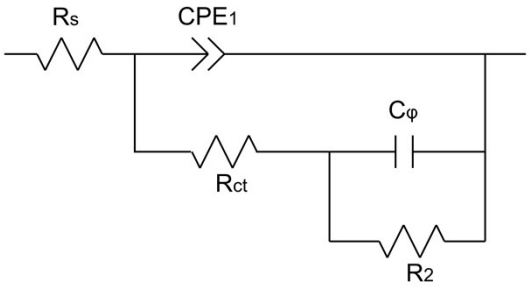

Fig. S29. The double-parallel equivalent circuit model for operando EIS measurements. R_2 and C_φ represent hydrogen adsorption resistance and capacitance, respectively.

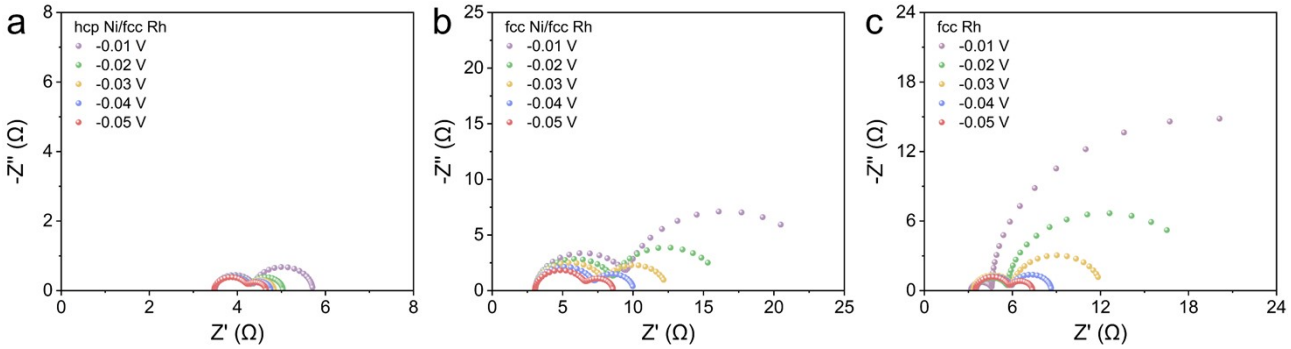

Fig. S30. Nyquist plots of (a) hcp Ni/fcc Rh, (b) fcc Ni/fcc Rh, and (c) fcc Rh at different potentials.

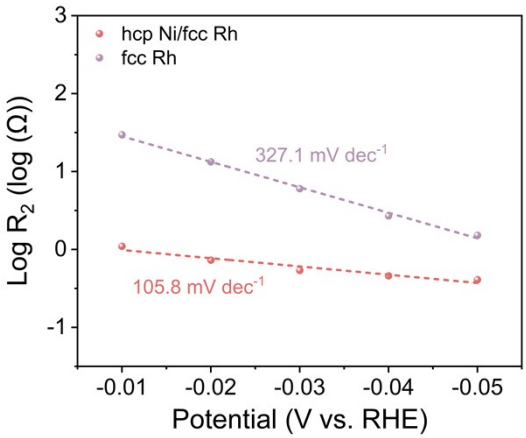

Fig. S31. Plots of logR_2 versus potential for hcp Ni/fcc Rh and fcc Rh.

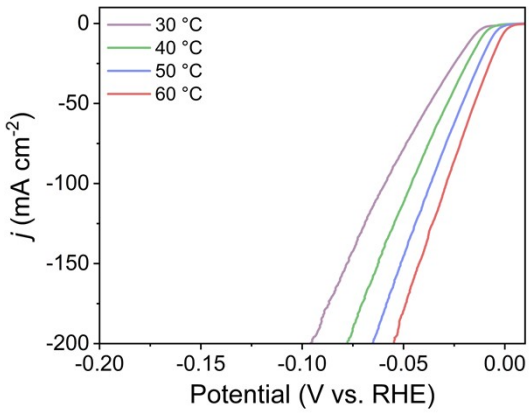

Fig. S32. Polarization curves of hcp Ni/fcc Rh at different temperatures ranging from 30 ℃ to 60 ℃.

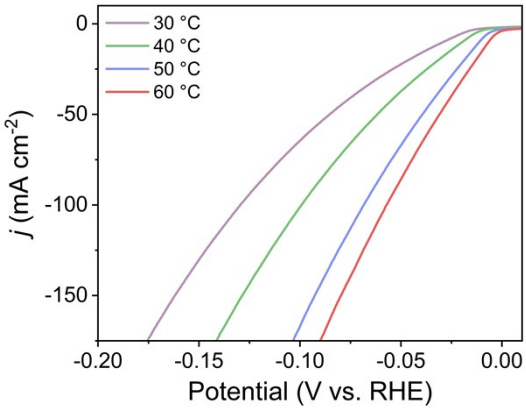

Fig. S33. Polarization curves of fcc Ni/fcc Rh at different temperatures ranging from 30 ℃ to 60 ℃.

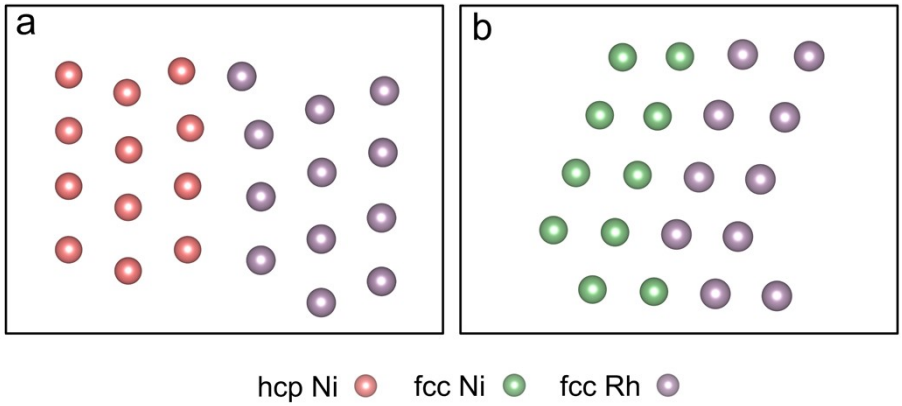

Fig. S34. Optimized structural models of (a) hcp Ni/fcc Rh and (b) fcc Ni/fcc Rh.

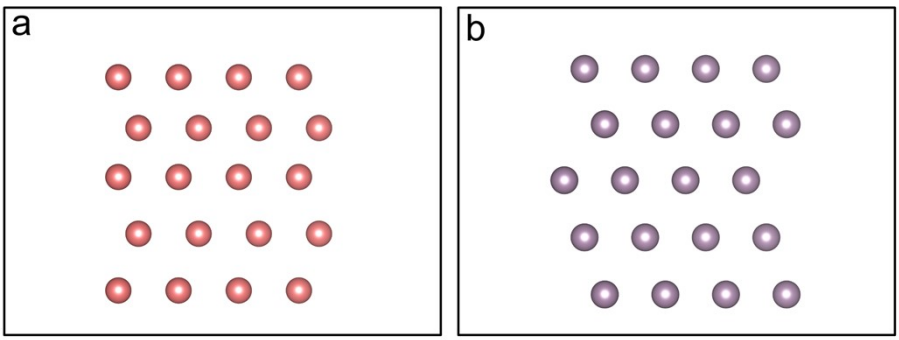

Fig. S35. Optimized structural models of (a) hcp Ni and (b) fcc Rh.

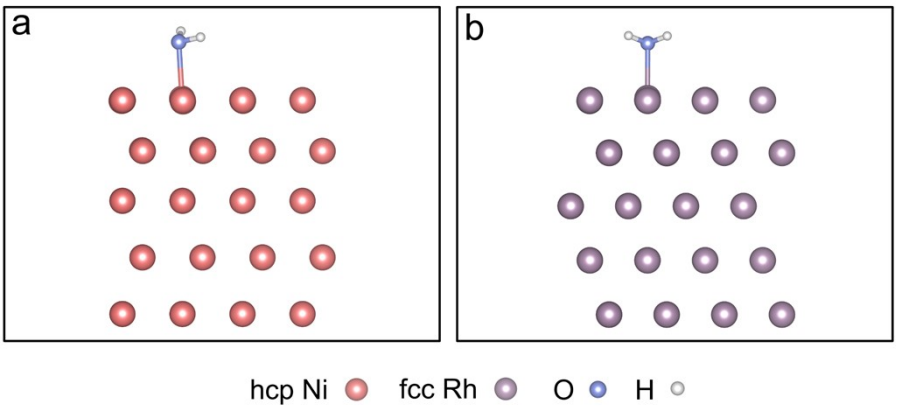

Fig. S36. Optimized structural models of water adsorption on (a) hcp Ni and (b) fcc Rh.

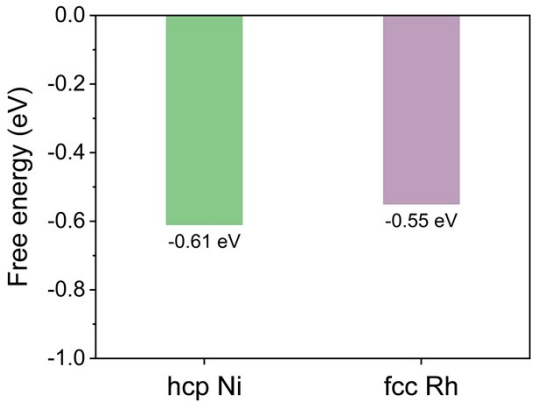

Fig. S37. The free energies of water adsorption on hcp Ni and fcc Rh.

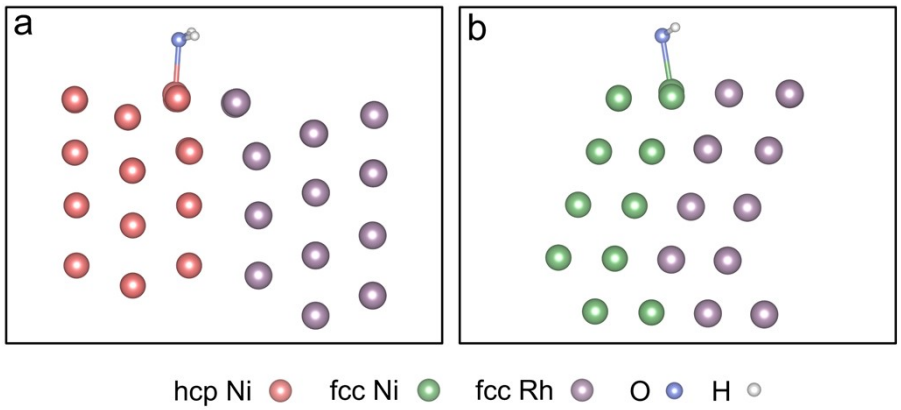

Fig. S38. Optimized structural models of water adsorption on (a) hcp Ni/fcc Rh and (b) fcc Ni/fcc Rh.

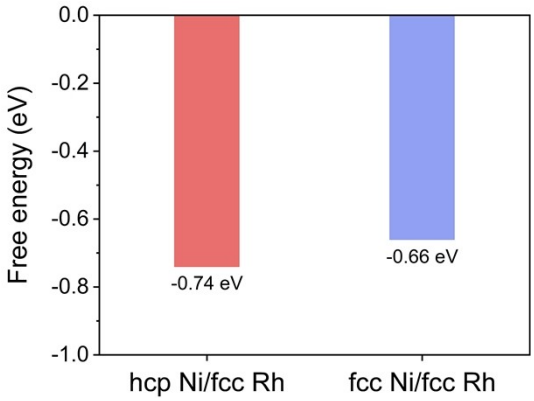

Fig. S39. The free energies of water adsorption on hcp Ni/fcc Rh and fcc Ni/fcc Rh.

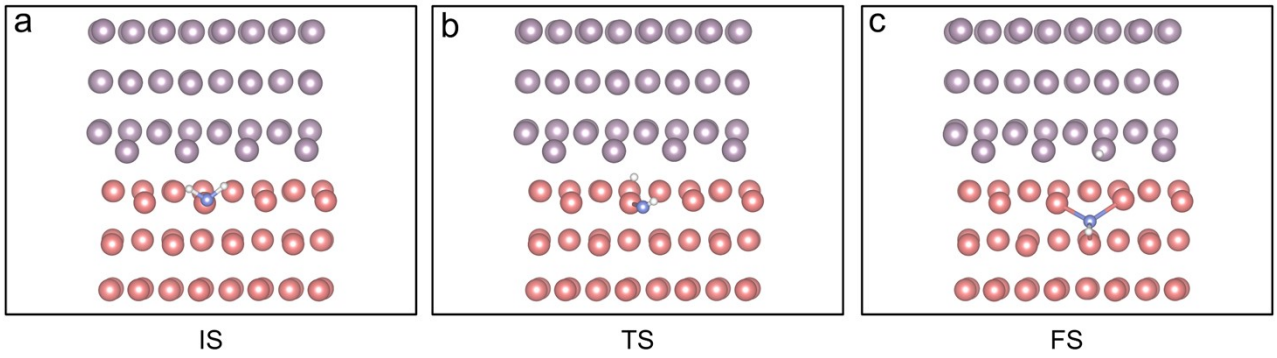

Fig. S40. Optimized structural models of water dissociation process on hcp Ni/fcc Rh. IS, TS, and FS represent initial state, transition state, and final state, respectively.

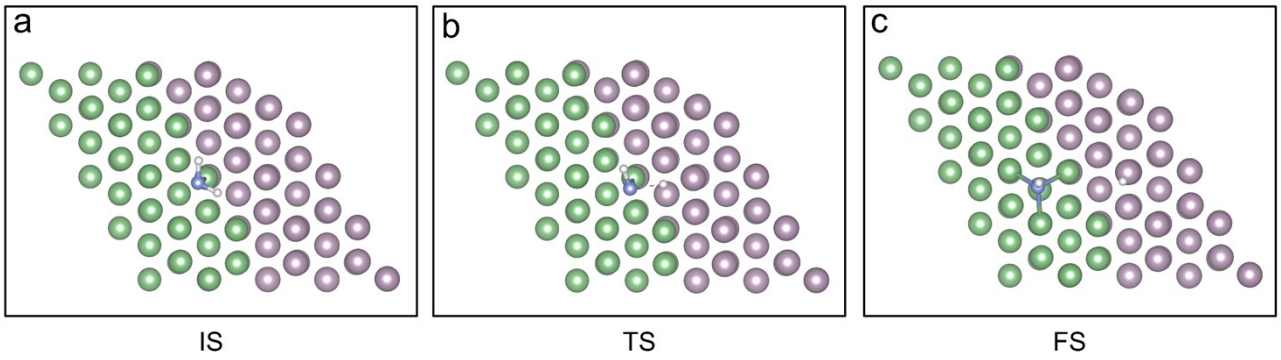

Fig. S41. Optimized structural models of water dissociation process on fcc Ni/fcc Rh. IS, TS, and FS represent initial state, transition state, and final state, respectively.

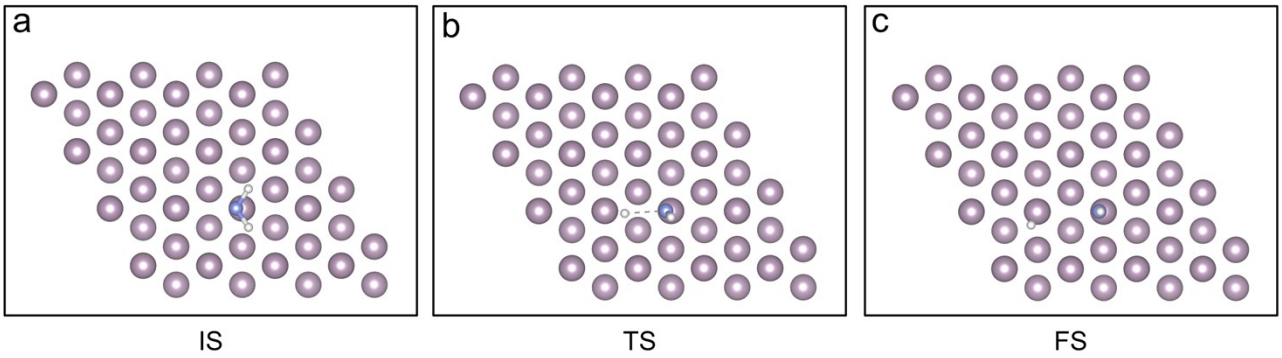

Fig. S42. Optimized structural models of water dissociation process on fcc Rh. IS, TS, and FS represent initial state, transition state, and final state, respectively.

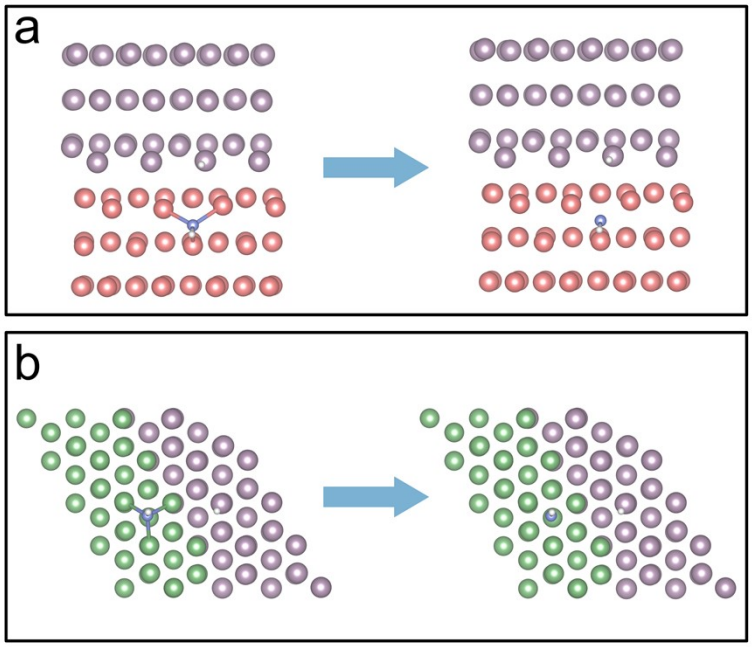

Fig. S43. Optimized structural models of *OH desorption process on (a) hcp Ni/fcc Rh and (b) fcc Ni/fcc Rh.

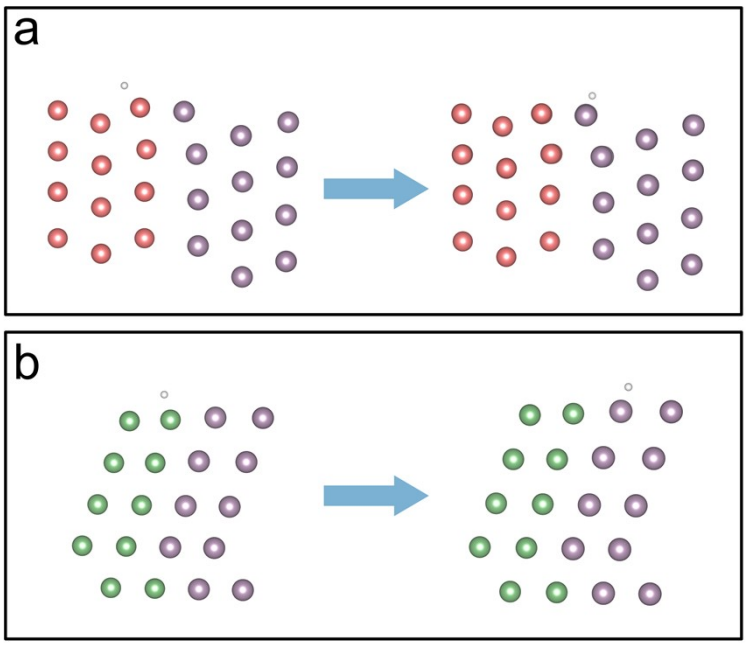

Fig. S44. Optimized structural models of *H transfer process from Ni site to Rh site on (a) hcp Ni/fcc Rh and (b) fcc Ni/fcc Rh.

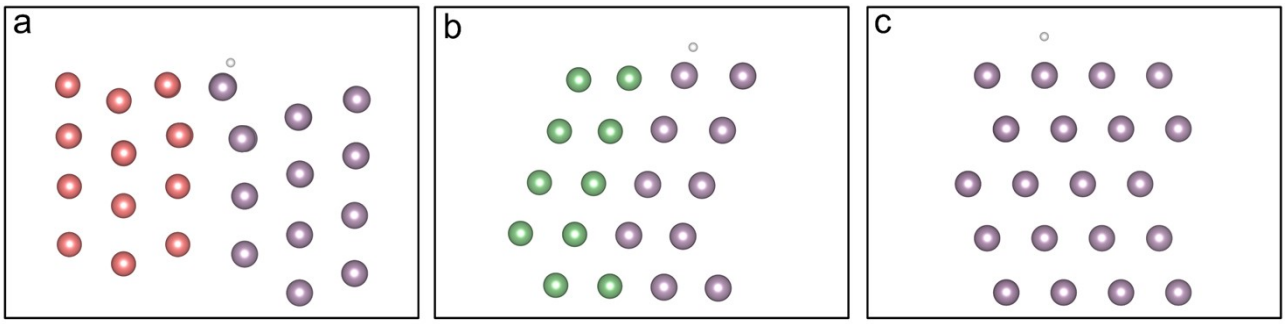

Fig. S45. Optimized structural models of hydrogen adsorption on (a) hcp Ni/fcc Rh, (b) fcc Ni/fcc Rh, and (c) fcc Rh.

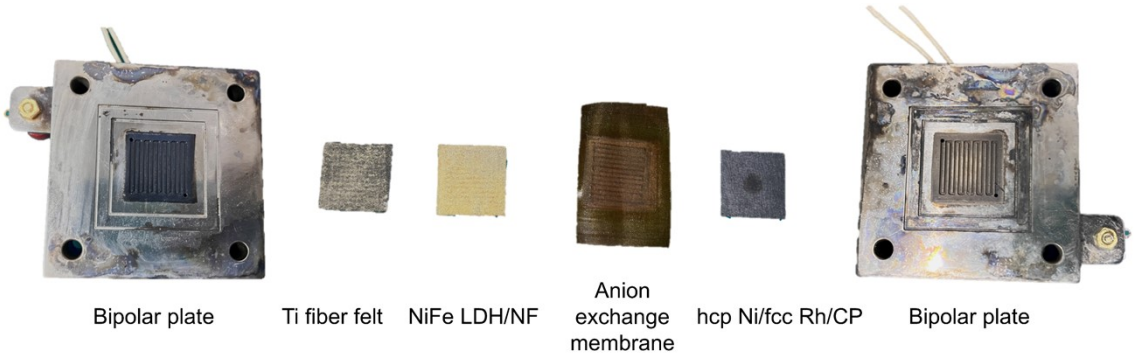

Fig. S46. Photograph of the components of AEMWE apparatus.

Fig. S47. Photograph of AEMWE setup.

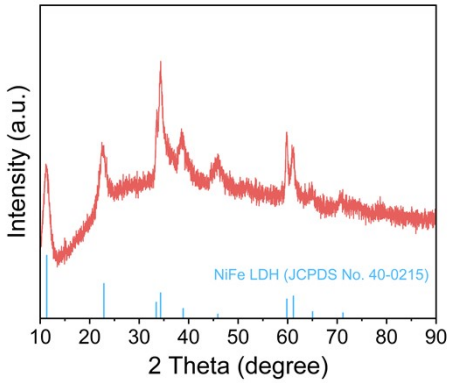

Fig. S48. XRD pattern of NiFe LDH.

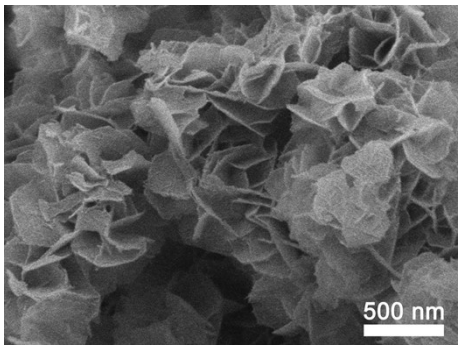

Fig. S49. SEM image of NiFe LDH.

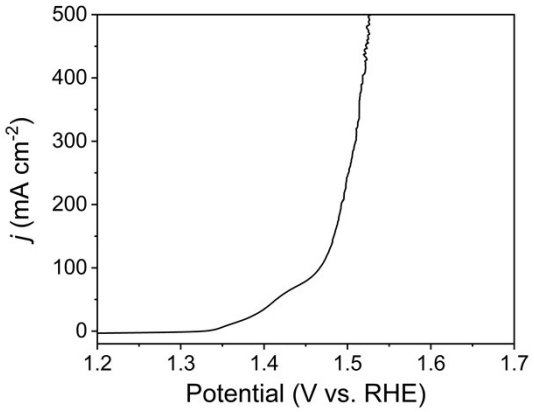

Fig. S50. Polarization curve of NiFe LDH.

Supplementary Tables

Table S1. Rh K-edge EXAFS fitting parameters.

Sample	Shell	CN	R (Å)	σ^2 (Å^2)	ΔE_0 (eV)	R factor
hcp Ni/fcc Rh	Rh-Ni	1.7±0.5	2.57±0.01	0.005±0.001	3.2±0.6	0.011
	Rh-Rh	9.1±0.7	2.68±0.00	0.004±0.000		
fcc Ni/fcc Rh	Rh-Ni	2.8±1.0	2.56±0.01	0.012±0.010	3.3±0.5	0.009
	Rh-Rh	9.7±0.7	2.68±0.01	0.004±0.000		
Rh foil	Rh-Rh	12	2.69±0.00	0.004±0.000	5.9±0.5	0.010
Rh_2O_3	Rh-O	6	2.01±0.02	0.004±0.001	-3.1±2.2	0.013

CN is coordination number. R is the distance between absorber and backscatter atoms. σ^2 is Debye-Waller factor to account for both thermal and structural disorders. ΔE_0 reflects inner potential correction. R factor indicates the goodness of the fitting.

Table S2. The comparisons of HER performance for hcp Ni/fcc Rh and other reported Rh-based catalysts.

Electrocatalyst	Electrolyte	Loading	Overpotential@ 10 mA cm^{-2} (mV)	Reference
hcp Ni/fcc Rh	**1.0 M KOH**	**38 μg_{Rh} cm^{-2}**	**20**	**This work**
Rh_{15}/NSC	1.0 M KOH	332 μg cm^{-2}	13.5	11
$Cs_3Rh_2I_9$/NC-R	1.0 M KOH	45 μg_{Rh} cm^{-2}	25	12
Rh/RhP_2@NPG	1.0 M KOH	300 μg cm^{-2}	21.3	13
Rh_2P{200}	1.0 M KOH	127 μg cm^{-2}	23	14
Rh-CoFe-ZLDH	1.0 M KOH	-	28	15
$Rh(OH)_3$/CoP	1.0 M KOH	20 μg_{Rh} cm^{-2}	13	16
Rh_2P	1.0 M KOH	19 μg_{Rh} cm^{-2}	30	17
Ni_xRh_{1-x}	1.0 M NaOH	620 μg_{Rh} cm^{-2}	37	18
Ni_1Rh_3	1.0 M KOH	142 μg_{Rh} cm^{-2}	75	19
RhPd-H	1.0 M KOH	15.3 μg_{Rh} cm^{-2}	40	20
Rh_6Cu_1 NPs	1.0 M KOH	51.2 μg_{Rh} cm^{-2}	36	21
PCN-$Rh_{15.9}$/KB	1.0 M KOH	40.6 μg_{Rh} cm^{-2}	25	22
$PtRh_{0.02}$@Rh NWs	0.1 M KOH	110 μg cm^{-2}	30.6	23
Rh/Pd metallene	1.0 M KOH	35.5 μg_{Rh} cm^{-2}	59	24
Rh/MoO_3	1.0 M KOH	14 μg_{Rh} cm^{-2}	29	25
Pt-Rhene	1.0 M KOH	124 μg_{Rh} cm^{-2}	37	26

Table S3. The ICP-OES results of hcp Ni/fcc Rh-1 h, hcp Ni/fcc Rh-3 h and hcp Ni/fcc Rh-5 h.

Sample	Rh (at%)	Ni (at%)
hcp Ni/fcc Rh-1 h	4.7	95.3
hcp Ni/fcc Rh-3 h	9.3	90.7
hcp Ni/fcc Rh-5 h	10.7	89.3

Table S4. The comparisons of AEMWE performance assembled by hcp Ni/fcc Rh and other reported advanced catalysts.

Electrocatalyst	Electrolyte	Temperature	Activity	Stability	Reference
hcp Ni/fcc Rh || NiFe LDH	**1.0 M KOH**	**50 ℃**	**1.73 V@500 mA cm^{-2} 1.83 V@1 A cm^{-2}**	**150 h@500 mA cm^{-2}**	**This work**
$CdNNi_3$ NS || Fe-$CdNNi_3$ NS	1.0 M KOH	80 ℃	1.96 V@1 A cm^{-2}	160 h@1 A cm^{-2}	27
Co-1T-MoS_2-bpe || NiFe LDH	1.0 M KOH	25 ℃	2.00 V@100 mA cm^{-2}	10 h@100 mA cm^{-2}	28
V-Ni_2P/$Ni_{12}P_5$ || NiFeCr	1.0 M KOH	55 ℃	1.79 V@500 mA cm^{-2}	40 h@500 mA cm^{-2}	29
Pt/C || NiCoFe NDA	0.1 M KOH	50 ℃	1.80 V@325 mA cm^{-2}	75 h@1.80 V	30
Cl-Pt/LDH || NiFe LDH	1.0 M KOH	60 ℃	1.87 V@1 A cm^{-2}	20 h@1 A cm^{-2}	31
Pt-AC/Cr-N-C || NiFe LDH	1.0 M KOH	80 ℃	1.78 V@500 mA cm^{-2}	100 h@500 mA cm^{-2}	32
Ir@Zr-CoP || Ir@Zr-CoP	1.0 M KOH	60 ℃	1.88 V@1 A cm^{-2}	150 h@500 mA cm^{-2}	33
Etched-NiPB@MS|| Etched-NiPB@MS	1.0 M KOH	25 ℃	1.98 V@1 A cm^{-2}	160 h@1 A cm^{-2}	34
B, V-Ni_2P || NiFeOOH	1.0 M KOH	55 ℃	1.78 V@500 mA cm^{-2}	100 h@500 mA cm^{-2}	35
np/Pt_1Ru_1-$Ni_{0.85}Se$ || np/Pt_1Ru_1-$Ni_{0.85}Se$	1.0 M KOH	60 ℃	1.84 V@1 A cm^{-2}	100 h@1 A cm^{-2}	36
Pt@S-NiFe LDH || S-NiFe LDH	1.0 M KOH	65 ℃	2.50 V@500 mA cm^{-2}	200 h@500 mA cm^{-2}	37

References

1. Y. Hong, S. Jeong, J. H. Seol, T. Kim, S. C. Cho, T. K. Lee, C. Yang, H. Baik, H. S. Park, E. Lee, S. J. Yoo, S. U. Lee and K. Lee, *Adv. Energy Mater.*, 2024, **14**, 2401426.
2. X. Ma, C. Ma, J. Xia, S. Han, H. Zhang, C. He, F. Feng, G. Lin, W. Cao, X. Meng, L. Zhu, X. Zhu, A.-L. Wang, H. Yin and Q. Lu, *J. Am. Chem. Soc.*, 2024, **146**, 20594-20603.
3. J. Huang, H. Sheng, R. D. Ross, J. Han, X. Wang, B. Song and S. Jin, *Nat. Commun.*, 2021, **12**, 3036.
4. L. Xiao, C. Cheng, T. Yang, J. Zhang, Y. Han, C. Han, W. Lv, H. Tan, X. Zhao, P. Yin, C. Dong, H. Liu, X. Du and J. Yang, *Adv. Mater.*, 2024, **36**, 2411134.
5. Z. W. Seh, J. Kibsgaard, C. F. Dickens, I. Chorkendorff, J. K. Nørskov and T. F. Jaramillo, *Science*, 2017, **355**, eaad4998.
6. B. Hammer, L. B. Hansen and J. K. Nørskov, *Phys. Rev. B*, 1999, **59**, 7413-7421.
7. G. Kresse and J. Furthmüller, *Phys. Rev. B*, 1996, **54**, 11169-11186.
8. J. He, L. Zeng, J. Li, D. Zhu, T. Gao, Y. Wang and Y. Chen, *Nano Energy*, 2024, **128**, 109894.
9. X. Tan, S. Geng, Y. Ji, Q. Shao, T. Zhu, P. Wang, Y. Li and X. Huang, *Adv. Mater.*, 2020, **32**, 2002857.
10. J. Wu, J. Fan, X. Zhao, Y. Wang, D. Wang, H. Liu, L. Gu, Q. Zhang, L. Zheng, D. J. Singh, X. Cui and W. Zheng, *Angew. Chem. Int. Ed.*, 2022, **61**, e202207512.
11. X. Bu, Y. Bu, Q. Quan, S. Yang, Y. Meng, D. Chen, Z. Lai, P. Xie, D. Yin, D. Li, X. Wang, J. Lu and J. C. Ho, *Adv. Funct. Mater.*, 2022, **32**, 2206006.
12. G. Lin, Z. Zhang, Q. Ju, T. Wu, C. U. Segre, W. Chen, H. Peng, H. Zhang, Q. Liu, Z. Liu, Y. Zhang, S. Kong, Y. Mao, W. Zhao, K. Suenaga, F. Huang and J. Wang, *Nat. Commun.*, 2023, **14**, 280.
13. Y. Liu, J. Ding, F. Li, X. Su, Q. Zhang, G. Guan, F. Hu, J. Zhang, Q. Wang, Y. Jiang, B. Liu and H. B. Yang, *Adv. Mater.*, 2023, **35**, 2207114.
14. S. Yang, X. Yang, Q. Wang, X. Cui, H. Zou, X. Tong and N. Yang, *Chem. Eng. J.*, 2022, **449**, 137790.
15. K. Zhu, J. Chen, W. Wang, J. Liao, J. Dong, M. O. L. Chee, N. Wang, P. Dong, P. M. Ajayan, S. Gao, J. Shen and M. Ye, *Adv. Funct. Mater.*, 2020, **30**, 2003556.
16. M. Xing, S. Zhu, X. Zeng, S. Wang, Z. Liu and D. Cao, *Adv. Energy Mater.*, 2023, **13**, 2302376.
17. F. Yang, Y. Zhao, Y. Du, Y. Chen, G. Cheng, S. Chen and W. Luo, *Adv. Energy Mater.*, 2018, **8**, 1703489.
18. D. Jin, A. Yu, Y. Lee, M. H. Kim and C. Lee, *J. Mater. Chem. A*, 2020, **8**, 8629-8637.

19. N.-A. Nguyen, V.-T. Nguyen, S. Shin and H.-S. Choi, *J. Alloys Compd.*, 2019, **789**, 163-173.
20. J. Fan, J. Wu, X. Cui, L. Gu, Q. Zhang, F. Meng, B.-H. Lei, D. J. Singh and W. Zheng, *J. Am. Chem. Soc.*, 2020, **142**, 3645-3651.
21. W. Zhang, J. Zhao, J. Zhang, X. Chen, X. Zhang and F. Yang, *ACS Appl. Mater. Interfaces*, 2020, **12**, 10299-10306.
22. H. Dong, Z. Zhao, Z. Wu, C. Cheng, X. Luo, S. Li and T. Ma, *Small*, 2023, **19**, 2207527.
23. X. Jiang, Z. Dong, Q. Zhang, G.-R. Xu, J. Lai, Z. Li and L. Wang, *J. Mater. Chem. A*, 2022, **10**, 20571-20579.
24. Z. Wang, G. Yang, P. Tian, K. Deng, H. Yu, Y. Xu, X. Li, H. Wang and L. Wang, *J. Mater. Chem. A*, 2023, **11**, 10222-10227.
25. J. Yuan, J. Feng, G. Li, Y. Song, N. Yu, X. Chen, G. He, Y. Tan and M. Ni, *Chem. Eng. J.*, 2025, **514**, 163260.
26. Q. Mao, W. Wang, K. Deng, H. Yu, Z. Wang, Y. Xu, X. Li, L. Wang and H. Wang, *J. Energy Chem.*, 2023, **85**, 58-66.
27. J. Zhang, Y. Tu, L. Zhang, S. He, C. Zhong, J. Ke, L. Wang, C. Cui, H. Song, L. Du and Z. Cui, *ACS Nano*, 2024, **18**, 32077-32087.
28. H.-J. Liu, S. Zhang, Y.-M. Chai and B. Dong, *Angew. Chem. Int. Ed.*, 2023, **62**, e202313845.
29. T. Zhao, S. Wang, Y. Li, C. Jia, Z. Su, D. Hao, B.-j. Ni, Q. Zhang and C. Zhao, *Small*, 2022, **18**, 2204758.
30. K. Yue, J. Liu, Y. Zhu, C. Xia, P. Wang, J. Zhang, Y. Kong, X. Wang, Y. Yan and B. Y. Xia, *Energy Environ. Sci.*, 2021, **14**, 6546-6553.
31. T. Zhang, J. Jin, J. Chen, Y. Fang, X. Han, J. Chen, Y. Li, Y. Wang, J. Liu and L. Wang, *Nat. Commun.*, 2022, **13**, 6875.
32. L. Zeng, Z. Zhao, Q. Huang, C. Zhou, W. Chen, K. Wang, M. Li, F. Lin, H. Luo, Y. Gu, L. Li, S. Zhang, F. Lv, G. Lu, M. Luo and S. Guo, *J. Am. Chem. Soc.*, 2023, **145**, 21432-21441.
33. Q. P. Ngo, T. T. Nguyen, Q. T. T. Le, J. H. Lee and N. H. Kim, *Adv. Energy Mater.*, 2023, **13**, 2301841.
34. J. Zhang, Q. Wu, J. Song, C. Xu, S. Chen and Y. Guo, *Nano Energy*, 2024, **128**, 109923.
35. T. Zhao, S. Wang, C. Jia, C. Rong, Z. Su, K. Dastafkan, Q. Zhang and C. Zhao, *Small*, 2023, **19**, 2208076.
36. L. Cai, H. Bai, C.-w. Kao, K. Jiang, H. Pan, Y.-R. Lu and Y. Tan, *Small*, 2024, **20**, 2311178.
37. H. Lei, Q. Wan, S. Tan, Z. Wang and W. Mai, *Adv. Mater.*, 2023, **35**, 2208209.